NUMERICAL STUDIES OF THE PASSAGE FLOWFIELD IN A 3-D TRANSONIC TURBINE BLADE CASCADE

Chang-Hsien Tai *

Vehicles Engineering Department
National Pingtung University of Science and Technology
Neipu Shiang 912, Pingtung, Taiwan, R.O.C.

Ding-San Wang ***

Department of Mechanical Engineering
National Taiwan University
Taipei, Taiwan 10617, R.O.C.

Ping-Hei Chen *

Uzu-Kuei Hsu ****

Department of Aircraft and Turbine
Air Force Aeronautical and Technical School
Gangshan, Kaohsiung, Taiwan 820, R.O.C.

Jr-Ming Miao **

Numerical Simulation Lab.
Chung Cheng Institute of Technology
National Defense University
Dashi Jen, Taoyuan, Taiwan 335, R.O.C.

ABSTRACT

A three-dimensional Navior-Stokes analyzer based on control volume method is developed to simulate the complex flow field within a turbomachinery. With VKI-CT2 turbine blade as the test model, numerical results are compared with experimented data and shows the existence of separation-transition bubble and the interaction of shock with turbulent boundary layer flow. The governing Navier-Stokes equations are solved by an improved numerical method that uses an upwind flux-difference split scheme for spatial descretization and an explicit optimally smoothing multi-stage scheme for time integration. Turbulent stresses are approximated by modifying Baldwin-Lomax algebraic, k-ε, R-k-ε and *RNG* k-ε turbulence models. According to the results of this research, this analyzer can indeed effectively modulate and simulate the aerodynamic characteristic of the transonic turbine rotor near the endwall.

Keywords : Transonic rotors, Separation bubble, Vortex, Endwall, CFD.

1. INTRODUCTION

The flow structure within the blade passage is very complex and hard to be predicted [1]. Larminar flow, transitional flow, turbulent flow, even the secondary flow caused by the spanwise pressure gradient between two adjacent blades can be observed. In some cases, there will be a separation bubble on the suction side or pressure side of a turbine blade surface. In dealing with this kind of problems, the geometry of blade's cylinder-like shape leading and trailing edge and the severe curvature variation within a small streamwise distance must be carefully considered.

The accuracy of prediction for turbine blade aerodynamics and heat transfer is determind by the accuracy in predicting the region of transition flow. The effect of a Mach number correction on a model for predicting the length of transition was investigated [2]. As discussed by Mayle [3], there is an extensive amount of experimental data showing the transition. A definite trend toward using Navier-Stokes solver to calculate these problems and the transport-equation turbulence closures, such as κ-ε, is demonstrated [4,5]. However, Larsson [6] compared two kinds of κ-ε and κ-ω turbulence models for the turbine blade. All models give oscillations at the separation point at the trailing edge. None of the models tested is able to predict suction-side transition correctly.

According to the above literature review, it is clear that different turbulence models need to be tested and three-dimensional effects should be included. In present study, an improved numerical approach is made to simulate the blade flowfield. An implicit multistage upwind flux-difference split scheme (Roe's scheme) coupled with different turbulence models including the modified Baldwin-Lomax [7], Launder-Sharma κ-ε [8], *RNG* κ-ε [9] and R-κ-ε [10] turbulence models has been developed to solve the steady Reynolds-averaged Navier-Stokes equations. To validate the code, a two-dimensional viscous flowfield analysis was characterized by complex phenomena of the blades

* Professor ** Associate Professor *** Candidate Ph.D. **** Drillmaster

passage flow interaction and Isentropic Mach number distribution. Comparing the results with experimental data, one finds fairly good agreement for the application of each of the different turbulence models mentioned.

2. COMPUTATIONAL GRID

Because of the complexity of leading edge, trailing edge, and near wall region, it is necessary to stretch grid in that region. Algebraically spaced grids are used to cover the flowfield, and the stretching transformation clusters using the Roberts [11] generalized stretching transformation technique are made near the boundary layer. The H-grid is used in the regions of upstream of the leading edge (Block I) and downstream of the trailing edge (Block III), and the O-grid is body-fitted to the surface of the blade (Block II), as shown in Fig. 1, so the multiblock grid approach is used in present study. The total number of cells is 826500 with respect to the 3-D blade as shown in Fig. 2. The steady-state solution was obtained by solving the time-dependent governing equations, and the residual is measured by the order of magnitude of the decay. The convergent solution was achieved when the residual had decayed by about 4 orders of magnitudes. Computation was performed on finer and coarser grids for a steady grid resolution; it was found that the total grid sizes, especially in the y direction, depend on the turbulence models used and those selected were chosen for suitability in comparing the accuracy of different turbulence models. According to present study, the average value of y^+ closest the surface is 0.2 with the exact solution for turbulence models [12]. The computational workstation is COMPAQ XP-1000.

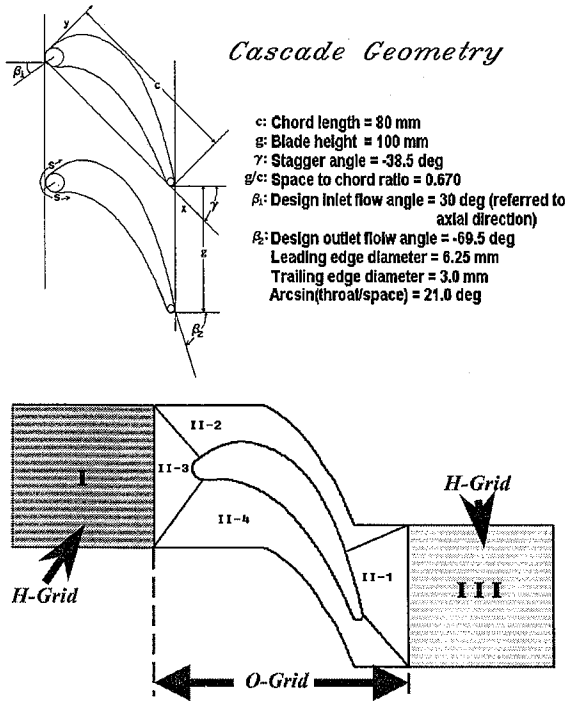

Fig. 1 Multiblock for the computational grid

Cells=826500

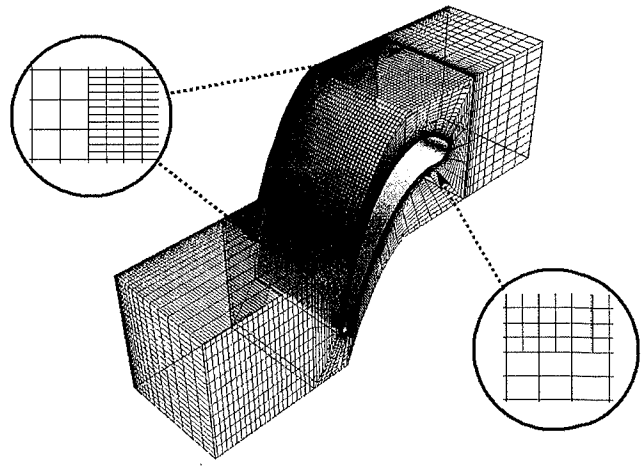

Block I = 25 × 25 × 20
Block II =
a) 226 × 32 × 80
b) 113 × 23 × 80
Block III = 43 × 32 × 20

Fig. 2 VKI-CT2 computational grid

3. GOVERNING EQUATION

The three-dimensional Renolds-averaged Navier-Stokes governing equations can be rewritten in a strong conservation form as:

$$\frac{\partial U}{\partial t}+\frac{\partial F}{\partial x}+\frac{\partial G}{\partial y}+\frac{\partial H}{\partial z}=0 \qquad (1)$$

where x is the streamwise direction, y is the pitchwise direction, and z is the spanwise direction

$$\mathbf{U}=\begin{bmatrix}\rho\\ \rho u\\ \rho v\\ \rho w\\ \rho E\end{bmatrix},\quad \mathbf{F}=\begin{bmatrix}\rho u\\ \rho u^2+p-\tau_{xx}\\ \rho uv-\tau_{xy}\\ \rho uw-\tau_{xz}\\ \rho uH^*-u\tau_{xx}-v\tau_{xy}-w\tau_{xz}+q_x\end{bmatrix}$$

$$\mathbf{G}=\begin{bmatrix}\rho v\\ \rho uv-\tau_{xy}\\ \rho v^2+p-\tau_{yy}\\ \rho vw-\tau_{yz}\\ \rho vH^*-u\tau_{xy}-v\tau_{yy}-v\tau_{yz}+q_y\end{bmatrix}$$

and

$$\mathbf{H}=\begin{bmatrix}\rho w\\ \rho uw-\tau_{xz}\\ \rho vw-\tau_{yz}\\ \rho w^2+p-\tau_{zz}\\ \rho wH^*-u\tau_{xz}-v\tau_{yz}-w\tau_{zz}+q_z\end{bmatrix}$$

where τ is the viscous stresses and q is the heat fluxes.

The equations are closed by the equation of state and constitutive relations for the coefficient of viscosity and the conductivity. The ideal gas equation of state was used with the specific heat ratio of 1.4 for air. The coefficients of viscosity in the above equations are obtained from Sutherland's law [11]. The conductivity is obtained by assuming a constant Prandtl number (Pr = 0.72 for air).

Based on the finite volume method, the governing equations can be described for a finite volume with an enclosing surface. It can thus be expressed in terms of the rate of changes in the average state U in the finite volume, and the surface integral becomes a sum of the fluxes over the six faces of a hexahedron. Consequently, Eq. (1) can be written in the normal flux form as:

$$\Delta\tilde{V}\frac{d\overline{U}}{dt}+\sum_{n=1}^{6}F_n\,\Delta A_n=0 \qquad (2)$$

where $\tilde{V}$ is the cell volume, and A_n is the cell surface area, and F_n is the flux normal to the cell surface, $F_n=\overline{F}\cos\alpha+\overline{G}\cos\beta+\overline{H}\cos\gamma$ with $\cos\alpha$, $\cos\beta$, and $\cos\gamma$ are the direction cosines of the n-th face.

4. BOUNDARY CONDITIONS

At solid wall boundary of the blade, the normal velocity is set equal to zero, since no mass or other convective flux can penetrate the solid wall. The other variables at the wall, such as pressure, velocity and temperature, have to be determined by extrapolation from the interior of computational region to the boundary, then the fluxes at the wall can be evaluated.

In the far field a characteristic analysis based on the Riemann invariant is used to determine the values of the flow variables on the outer boundary of the grid. This analysis correctly accounts for wave propagation in the far field which is important for achieving rapid convergence to a steady state.

5. NUMERICAL METHODS

The use of upwind difference schemes for solving the Euler and Navier-Stokes equations is becoming popular for several reasons [13,14]. For example, upwind schemes have natural numerical dissipation, better stability properties, and more accurate results. Furthermore, if techniques such as multigrid strategies, vector and parallel architectures, and local grid refinement are to be used, then the explicit scheme is preferred. Consequently, the explicit multi-stage Roe's flux-difference splitting scheme [13,15,16], which can be applied to the conservation law and accurately represent the boundary layer, is chosen as the particular upwind method used here.

Equation (2) can be rewritten as:

$$\frac{d\overline{U}}{dt}+\frac{1}{\Delta\tilde{V}}\sum_{n=1}^{6}F_n\,\Delta A_n=0 \qquad (3)$$

in which the flux vector F_n can be expressed as the sum of an inviscid and a viscous/conductive part:

$$F_n=F_n^i+F_n^\mu \qquad (4)$$

The inviscid fluxes are approximated through a flux splitting scheme (Roe's scheme), and the viscous fluxes are approximated through central differencing.

The basic method of inviscid flux computation based on Roe's approximated Riemann solver [17] for the Euler equations is essentially the same for both grid-aligned and grid-independent schemes. The modified absolute velocities enforce the entropy condition, which eliminates expansion shocks, and ensures a smooth transition from subsonic to supersonic flow.

6. HIGH-RESOLUTION SCHEME

A first-order scheme is initially applied, so the left and right states are chosen to be the cell average values to the left and right of the cell faces. In a high-resolution scheme, in order to raise the order of accuracy of upwind differencing, all one needs to do is to raise the order of accuracy of the initial-value interpolation that yields the zone-boundary data. Such schemes are labeled as high resolution schemes as opposed to Total Variation Diminishing (TVD) schemes, which completely eliminate any of those spurious oscillations when applied to one dimensional nonlinear hyperbolic conservation laws and linear hyperbolic systems. The van Leer kappa-scheme, in which the kappa number is one-third, was selected to obtain a high-resolution upwind differencing [18~21].

An optimal multi-stage scheme is used for the time integration, the multi-stage coefficients are modified by Tai [14] and redefined using the Courant number for multi-dimensional use. Also, a residual smoothing method is imposed to accelerate convergence and to improve numerical stability.

7. TURBULENCE MODELS

In this section we describe the turbulence models used in the present study.

7.1 Baldwin-Lomax Algebraic Turbulence Model [7]

In the algebraic turbulence model, the effects of turbulence are simulated in terms of an eddy viscosity coefficient μ_t. Thus, in the stress terms of the laminar Navier-Stokes equations, the molecular coefficient of viscosity μ is replaced by $\mu_{iam}+\mu_t$. This model avoids the necessity for finding the edge of the boundary layer, but it seems that it can not properly simulate the

separated flow regions, and only provides satisfactory results for relatively simple flow geometries.

7.2 Launder-Sharma Two-Equation Turbulence Model [8]

In our work, the Launder-Sharma k-ε model is used since it does not require knowledge of the grid-point distance from the solid boundaries. The values of the eddy viscosity and eddy conductivity are estimated by solving two transport equations for the turbulent kinetic energy κ and its dissipation rate ε. There is no substantial Reynolds-number restriction since the turbulence closure used is well-adapted to transitional flows, as well as fully turbulent ones. For higher Mach number values, the effects of compressibility on turbulence become dependent upon the density fluctuations. Therefore, it is restricted to the Mach-number range from M = 0 to M = 5, and is unable to predict some well-documented features of simple shear flows.

7.3 *RNG* k-ε Two-Equation Turbulence Model [9]

The ε-equation has long been suspected as one of the main sources of accuracy limitations for the standard version k-ε model [22]. It is, therefore, interesting to note that the model contains a strain-dependent correction term in the constant $C_{\varepsilon 1}$ of the *RNG* model standard ε-equation. The model can be applied with the isotropic Reynolds stress formula or with the non-linear form.

7.4 *R-k*-ε Three-Equation Turbulence Model [10]

The approach extends the standard k-ε model [22] to low Reynolds number flow regimes by combining it with the pointwise k-R model of Goldberg [23] so that no explicit wall distance is needed, rendering the model applicable to arbitrary geometries. This version has the following attributes: (a) it does not involve wall distance or normal-to-wall directionality; (b) it enforces time scale realisability by preventing it from falling below the Komogorov (disspative eddy) scale, $(\nu/\varepsilon)^{1/2}$; (c) it employs a simple wall boundary condition for ε.

8. RESULTS AND DISCUSSION

The thermal design of turbine blade is influenced by the flow transition phenomenon inside the boundary layer [3]. The effect of a Mach number correction on a model for predicting the length of transition was investigated [3]. The transition length decreases as the turbulent spot production rate increases [24]. Recent data and analysis showed that the spot production rate is effected by Mach number [25~27].

8.1 Comparision of the Turbulence Models

The VKI-CT2 rotor has the following attributes: (a) separation bubble near the leading edge of the suction side, (b) shock. Figure 3 shows the comparision of measured and predicted isentropic surface Mach number for VKI-CT2 rotor. In the suction side, 0.003 < X/C < 0.3, there is a separation bubble. Separation comes from the shape of the leading edge changed as shown in Fig. 4. Because of the pitchwise pressure gradient, as shown in Fig. 5, the flow through the pressure side is flowing forward the suction side, then the flow is accelerated and the separation flow is reattached. On the blade surface, therefore, a separation bubble is formed. The flow in this region is slow, but has longer separation length. Because of large pitchwise pressure, the anti-flow of the top suction side is increased inside the separation bubble as shown in Fig. 4. The Baldwin-Lomax and *RNG* κ-ε turbulence models matches very well as shown in Fig. 3(a) and 3(b) (X/C ≅ 0.2), but κ-ε turbulence model match poor in this region as shown in Fig. 3(b) (X/C ≅ 0.2).

Because of pitchwise pressure gradient and converge passage, the shock occurred as shown in Fig. 3 and Fig. 5 (X/C ≅ 5.8). Behind the shock, The flow speed is decreased and pressure is increased and the slope of the blade shape is intensely changed. Therefore, the separation occurred again as shown in Fig. 6. The shock is an intense phenomenon, and the pressure gradient is increased behind it. For this reason, the *RNG* κ-ε turbulence model is correct as shown in Fig. 3(d) (X/C ≅ 0.6), but the Baldwin-Lomax and κ-ε turbulence model is incorrect in this region as shown in Fig. 3(a) and 3(b) (X/C ≅ 0.6) respectively.

Because of the curvature of the trailing edge is intensely changing, the trailing vortex is occurred. The region of the shock and trailing edge form into a local low pressure region. Because the exit angle is different between the pressure side and suction side, the joint flow is slowly behind the trailing edge. Therefore, it forms into a local high pressure region. The flow of suction side through the shock is increased because the large pressure gradient occurred by the local high pressure behind the trailing edge. For this reason, the trailing vortex forms into a pair of long and small vortices as shown in Fig. 7. Because of the local high pressure region of the trailing edge, it forms into a pitchwise pressure region for the next blade. The speed of the flow is increased in this region. Comparing the simulation with the experimental data in this region, the *RNG* k-ε turbulence model fits very well as shown in Fig. 3(d) (X/C ≅ 0.6 ~ 0.7).

8.2 Separation Bubble Flowfield Analysis

The design inlet angle of the VKI-CT2 blade is 30°. Figure 8(a) shows the distribution of the surface isentropic Mach number with inlet angle of 30°. There is only small separation bubble occurred as shown in Fig. 9. The reason is the inlet flow that occurred by the low pitchwise velocity, high streamwise velocity, and pitchwise pressure gradient.

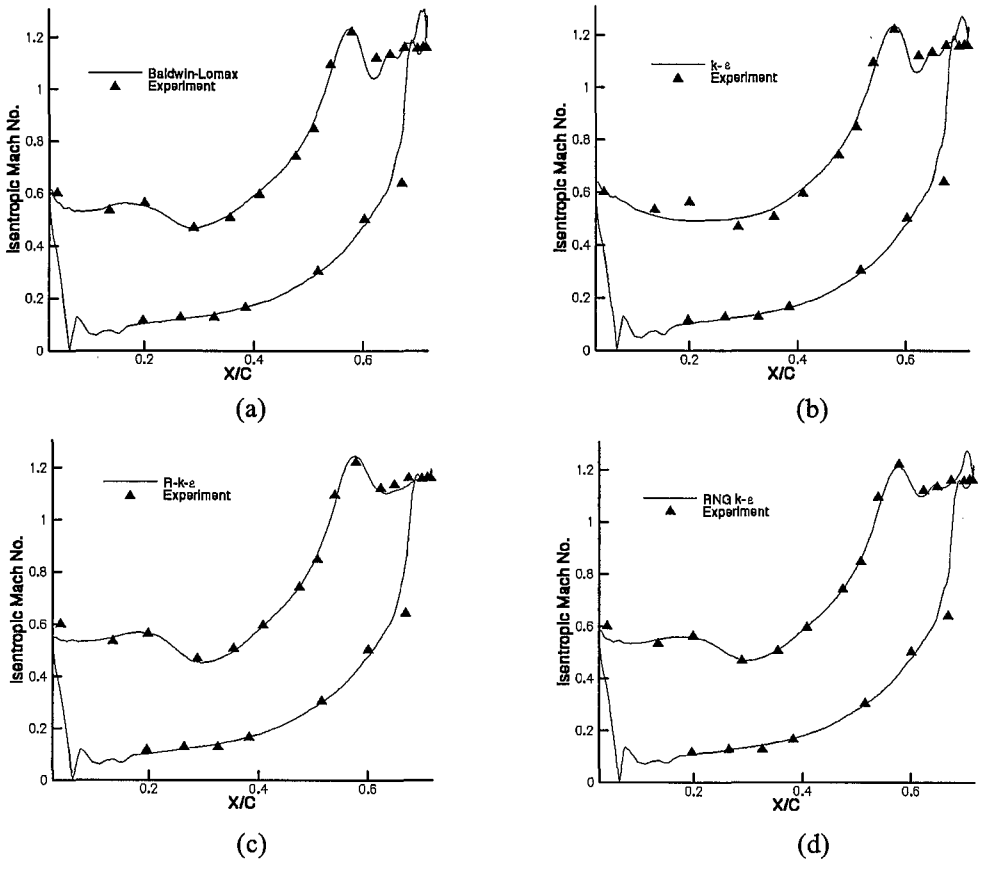

Fig. 3 Isentropic Mach no. along the surface with inlet angle of 45°

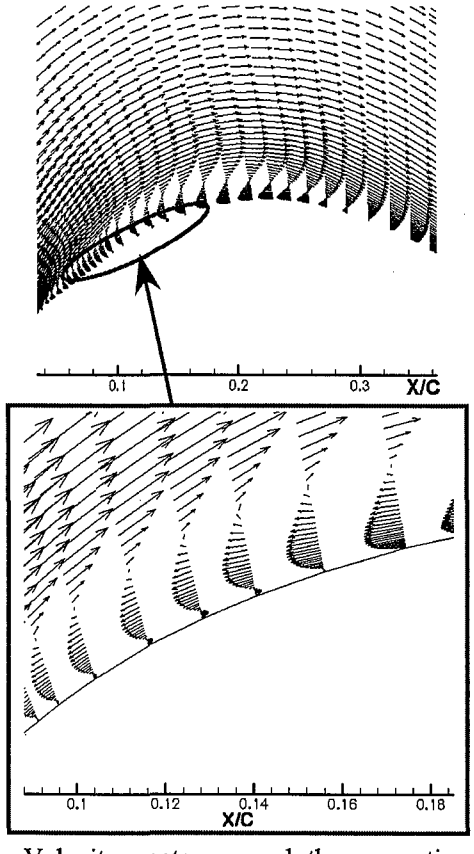

Fig. 4 Velocity vector around the separation region with inlet angle of 45°

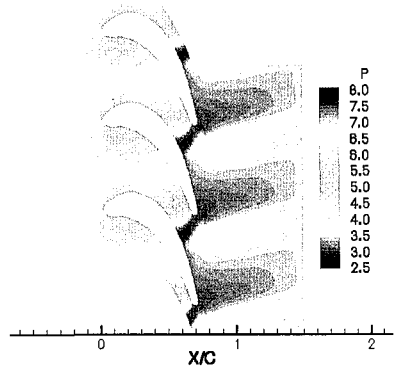

Fig. 5 Dimensionless pressure distribution with inlet angle of 45°

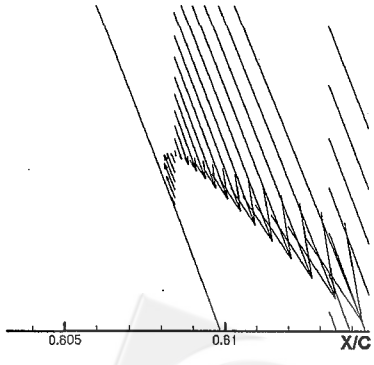

Fig. 6 Velocity vector behind the shock of the suction side with inlet angle of 45°

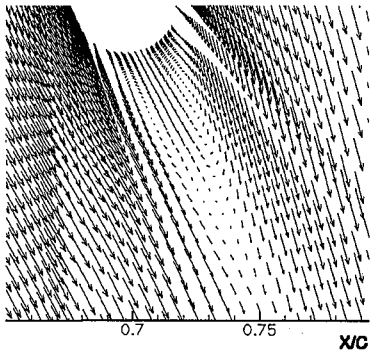

Fig. 7 Velocity vector around the trailing edge with inlet angle of 45°

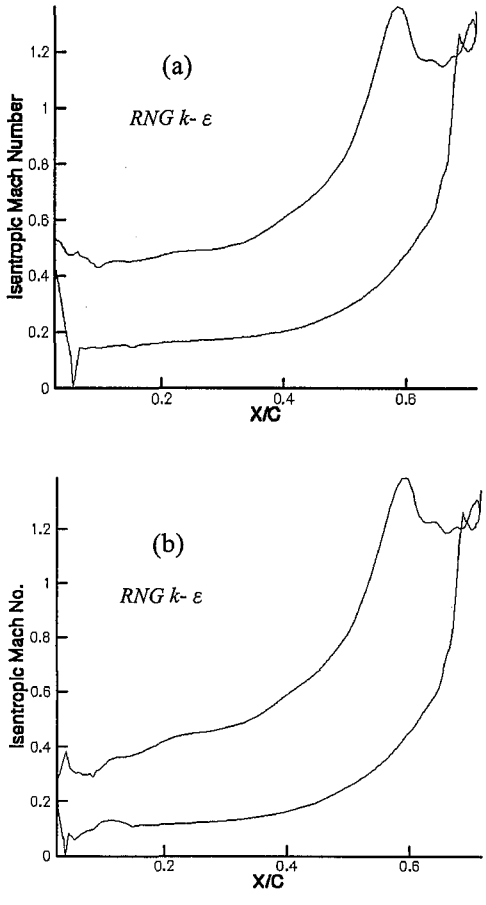

Fig. 8 Isentropic Mach no. along the surface (a) inlet angle of 30°, (b) inlet angle of 15°

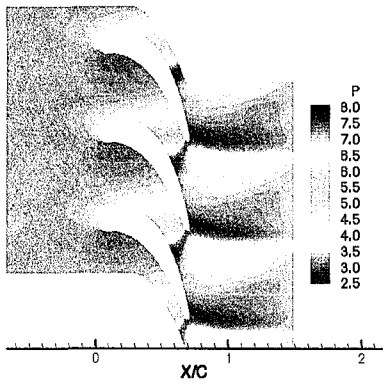

Fig. 9 Dimensionless pressure distribution with inlet angle of 30°

For this reason, the separation is reattached at X/C ≅ 0.095 as shown in Fig. 8(a). For the inlet angle of 45°, the separation is larger because it has higher pitchwise velocity, and the separation is also reattached by the pitchwise-pressure gradient as shown in Fig. 3(d) (X/C ≅ 0.3). Therefore, there is a large separation bubble in this region. In the separation bubble, the speed of the anti-flow is increased by the secondary flow which occurred by pitchwise pressure gradient and the curvature of the blade. Therefore, the separation of the anti-flow occurred at X/C ≅ 0.18 as shown in Fig. 4, and stopped by the pressure region which occurred by the separation bubble, and there is another short separation bubble. According to the distribution of the isentropic Mach number, the onset and end of the transition region of the separation bubble [3] which defined as shown in Fig. 10 are the end and onset of the short separation bubble at about X/C = 0.09 and 0.18 as shown in Fig. 3(d). The heat dissipation of this region is poor in actual application, and the blade may be to burn down. If inlet angle is 15°, the separation bubble is not occurred as shown in Fig. 8(b).

The region of the separation bubble is also affected by the turbulent intensity as shown in Fig. 11. When the inlet angle is 30°, the X_T (the end of the transition) is the point A for Tu = 3%, and the X_T is the point B for Tu = 6% and 9%, as shown in Fig. 11(a). When the inlet angle is 45°, the X_T is the point A for Tu = 3%, and the X_T is the point B for Tu = 6% and 9%, as shown in Fig. 11(b). It shows that, the end of the transition is affected by the turbulent intensity in a separation bubble. When the turbulent intensity is increased, the X_T moves forward, and more obviously. However, the X_T is limited when the turbulent intensity decreased.

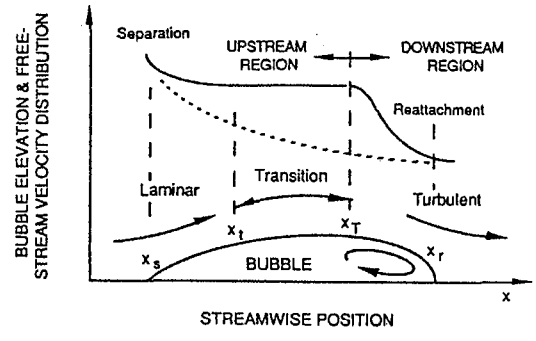

Fig. 10 Flow around a separation bubble and corresponding free-stream velocity distribution [3]

8.3 The Stagnation Point Flowfield Analysis

The pressure is the highest and the velocity is zero in the stagnation point. Therefore, the heat dissipation of this region is poor in actual application. It is usually to use the film cooling to protect. Because of higher streamwise velocity and lower pitchwise velocity, the flow speed is increased along to the down stream of the leading edge with inlet flow angle of 15°. The curvature of the blade is not changed until X/C = 0.12,

and the secondary flow occurred by the pitchwise pressure which occurred in the inlet flow. For this reason, the flow slows down between X/C = 0.12 and X/C = 0.4, and this property is also the same with inlet angle of 30° or 45°.

8.4 The Trailing Edge Flowfield Analysis

Because the shape of the trailing edge is a cylinder, the vortex region occurred. The heat dissipation is poor in this region and the blade may be burn down. It is usually to use film cooling to protect. The pitchwise velocity is offset by joint flow of the trailing edge because the flow speed and exit flow angle is not the same between the upstream and downstream. Therefore, a local high pressure region occurred. A pitchwise pressure region occurred by the local high pressure for the next level blade, and a physical passage, converge-diverge passage, occurred on the suction side. Therefore, the flow speed through the shock is decreased first and then increased again. The separation phenomenon is increased because the slope of the blade shape is increased in this region. The flow of the suction side that is close-by the trailing edge is jointed by the flow of the above level blade, and the flow speed is increased till the cylinder region of the trailing edge.

8.5 The Endwall Flowfield Analysis

According to the experimental research [28], Figure 12 shows the flowfield of a blade near the wall. The flow through the leading edge of the endwall exists a couple of horseshoe vortices, and the two horseshoe vortices are combined in passage vortex in the blade passage. Because of momentum balance, the corner vortex occurred in the suction side, pressure side and leading edge of the endwall. According to the simulation of this study, there are a couple of horseshoe vortices as shown in Fig. 13. Because of wall effection, the horseshoe vortices are close-by the endwall. However, the spanwise flow is occurred by the pressure gradient in the blade passage, and the horseshoe vortices are removed from the endwall. To combine with Fig. 14, the local high pressure region of the suction side is the flowing direction of the horseshoe vortex. The local high pressure regions of the trailing edge of the suction side and pressure side are caused by the corner vortex near the endwall. The local high pressure regions of the leading edge are also caused by the corner vortex. Figure 15 shows the corner vortex near the endwall. The source of the corner voetex is not the only one from the numerical simulation, especially along the pressure side. In addition, the

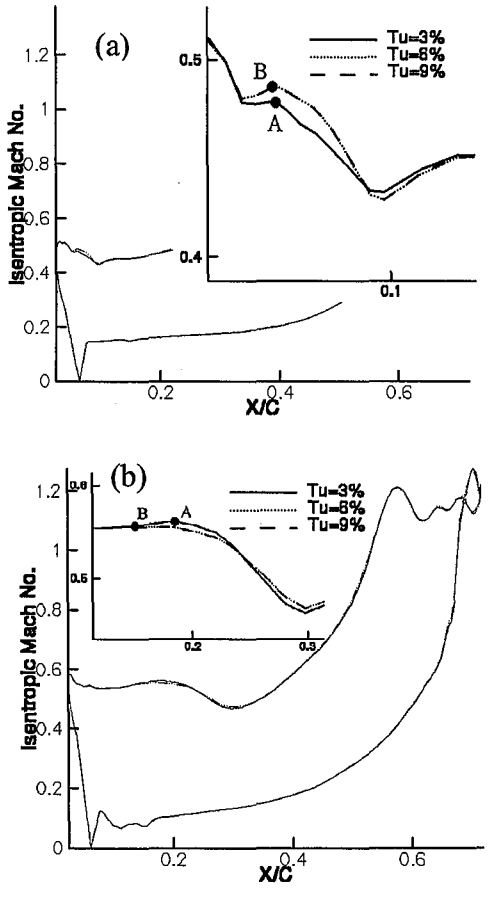

Fig. 11 Isentropic Mach no. along surface with different Tu (a) Inlet angle of 30°, (B) Inlet angle of 45°

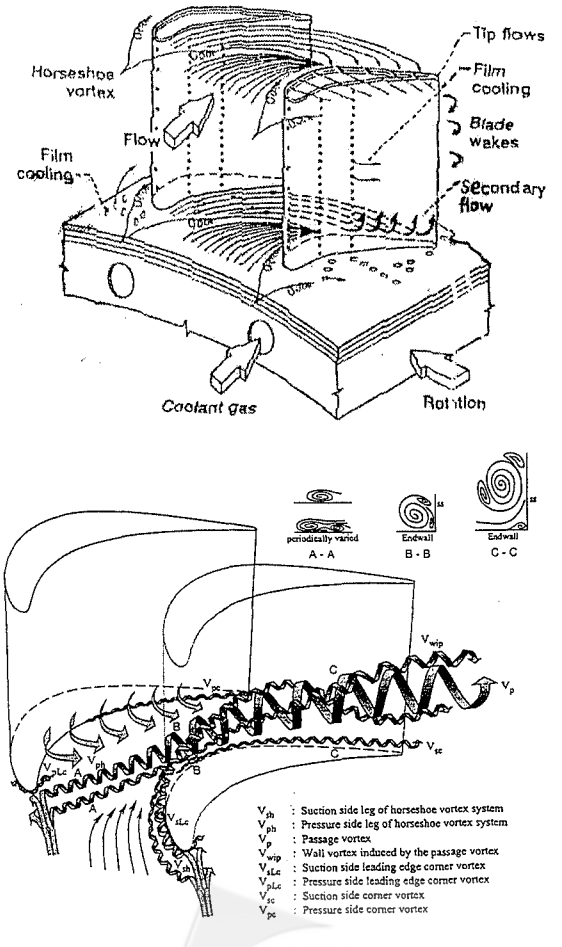

Fig. 12 Interpretation of the vortex flow pattern [1,28]

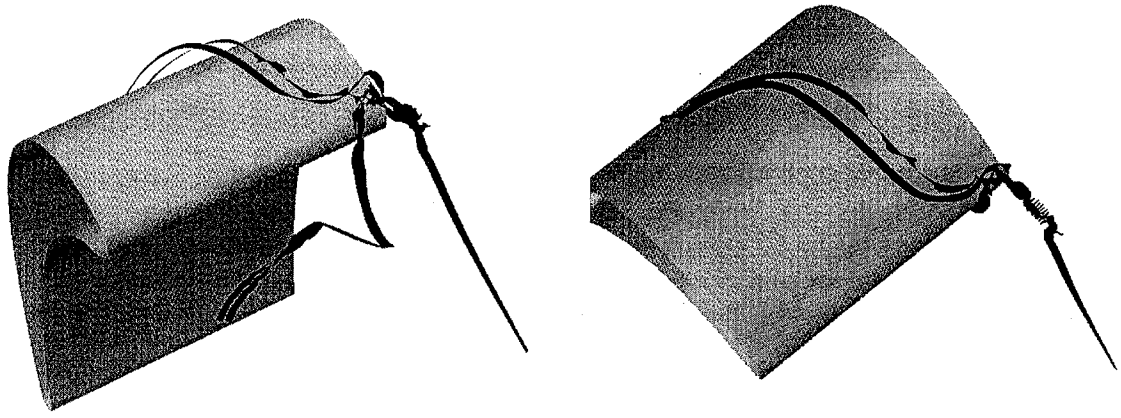

Fig. 13 The stream line of the horseshoe vortex

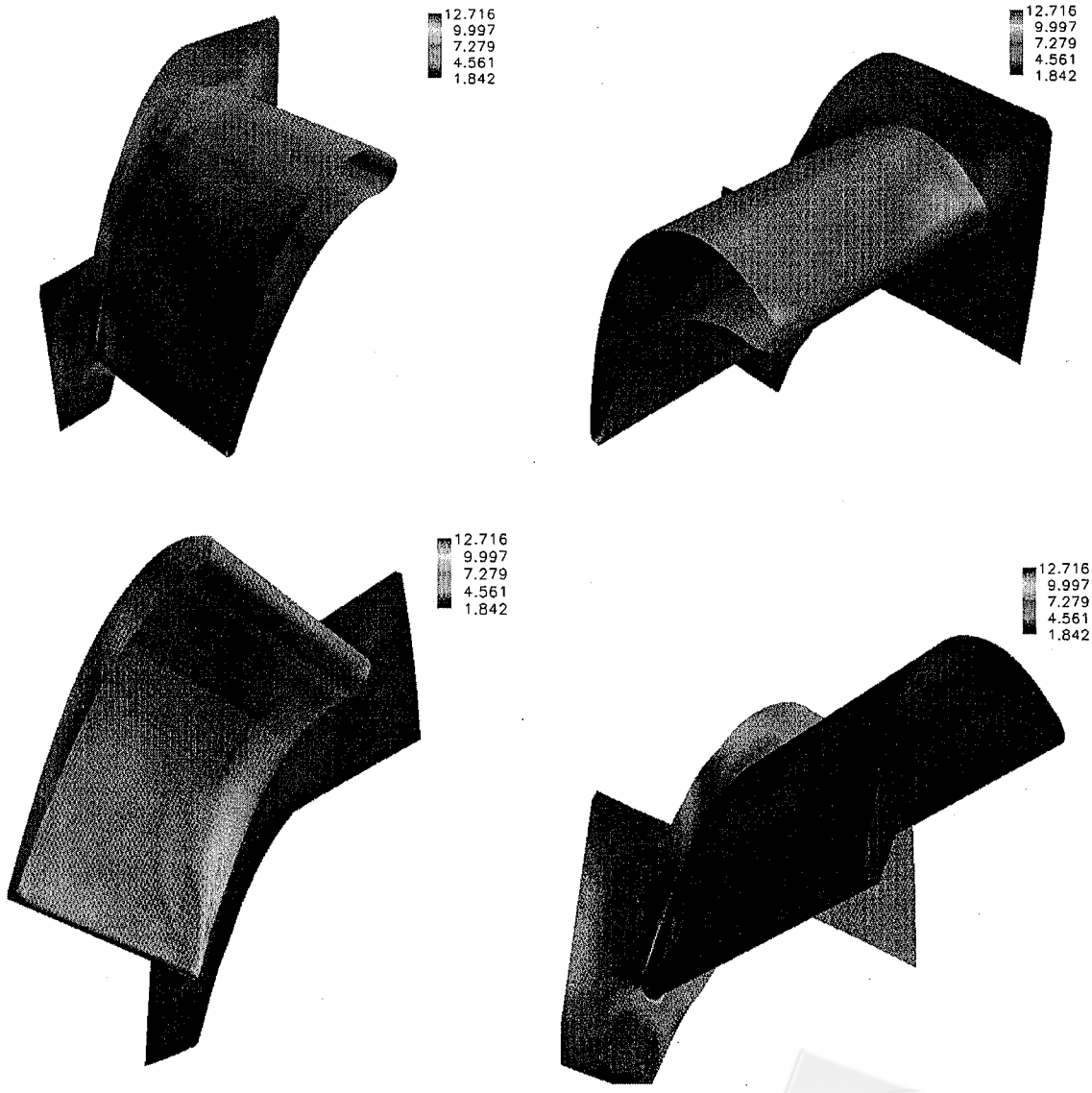

Fig. 14 Dimensionless pressure distribution with inlet angle of 45°

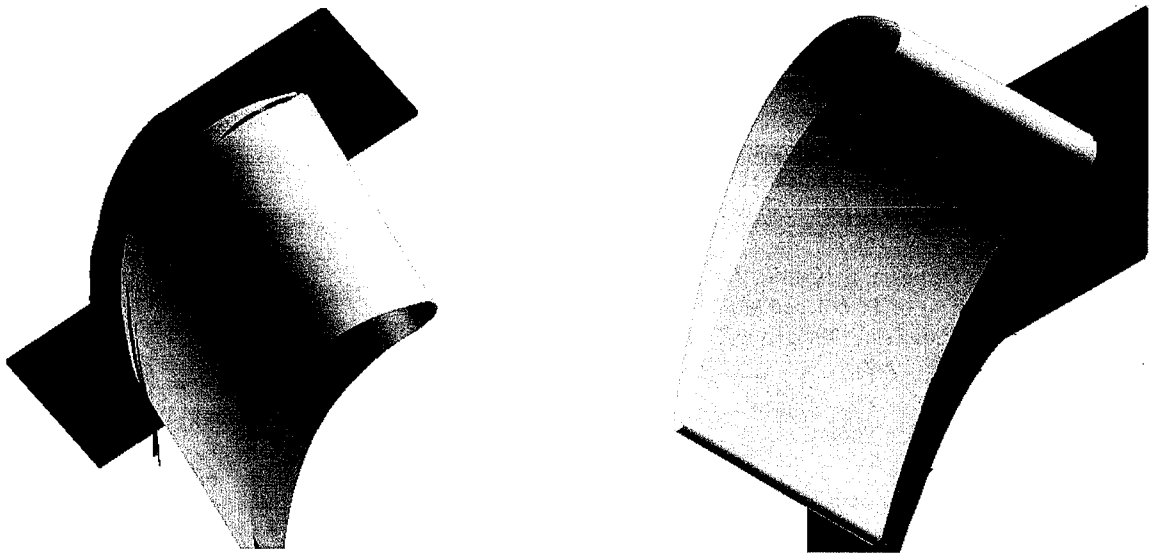

Fig. 15 Corner vortex near the endwall

passage spread is not the same so that the pithwise pressure gradient is different. Near the tailing edge on the pressure side, the pithwise pressure gradient is little so that the corner vortex can hit the blade. For this reason, the high pressure region occurred in the trailing edge as shown in Fig. 14. Figure 16 shows the streamline through the separation bubble region. The longer is the distance from the endwall, the smaller is the size of the bubble. Therefore, the airflow is around the separation until the distance from the endwall is getting longer.

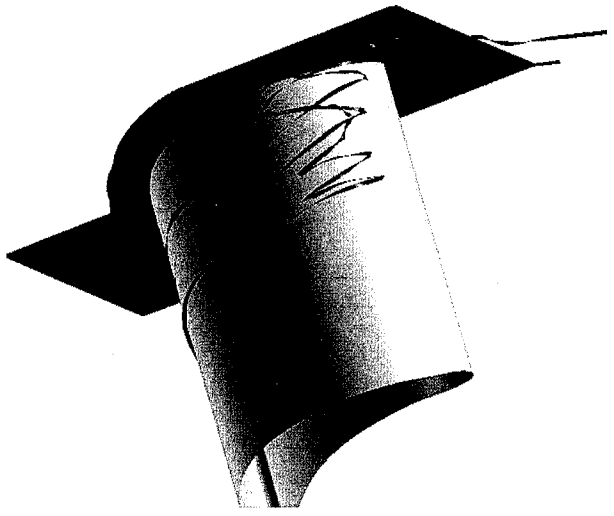

Fig. 16 Separation bubble streamline near the endwall

9. CONCLUSIONS

(1) In this study, it is effectively to simulate the complex flow phenomena on transonic turbine blade by using the advanced numerical methods and second order enclosure turbulence models.
(2) Among turbulence model tested in present study, the optimal selection for the transonic blade is the RNG k-ε turbulence model.
(3) The length of separated-transition bubble on the suction side of test blade is directly related to the inlet angle at the test conditions.
(4) Increasing the turbulence level results in forward motion of end point of separation transition bubble for some test cases.
(5) There is a short separation bubble just occupied within the separation bubble for larger inlet angle. In addition, the onset and end of the short bubble is just about the onset and end of the transition with the separation bubble.
(6) The separation is induced by the passage shock on the suction side.
(7) The size of the bubble is inverse proportional to the distance from the endwall.

REFERENCES

1. Simoneau, R. J. and Simon, F. F., "Progress Towards Understanding and Predicting Heat Transfer in the Turbine Gas Path," *Int. J. Heat and Fluid Flow*, 14(2), pp. 106–128 (1993).
2. Boyle, R. J. and Simon, F. F., "Mach Number Effects on Turbine Blade Transition Length Prediction," ASME Paper, 98-GT-367 (1998).
3. Mayle, R. E, "The Role of Laminar-Turbulent Transition in Gas Turbine Engines," *J. of Turbomachinery*, 113, pp. 509–537 (1991).
4. Lakshminarayana, B., "Turbulence Modeling for Complex Shear Flow," *AIAA J.*, 24(12), pp. 1900–1917 (1986).
5. Leschziner, M. A., "Computation of Aerodynamic Flows Turbulence-Transport Models Based on 2-Moment Closure," *Computers Fluids*, 24(4), pp. 377–392 (1995).
6. Larsson, J., "Turbine Blade Heat Transfer Calculations Using Two-Equation Turbulence Models," *Proc. Instn.*

Engrs., 211(A), pp. 253–262, A01897 (1997).

7. Degani, D. and Schiff, L. B., "Computation of Supersonic Viscous Flows Around Pointed Bodies at Large incidence," AIAA Paper 83-0034 (1983).
8. Launder, B. E. and Sharma, B. I., "Application of the Energy Dissipation Model of Turbulence to the Calculation of Flow Near a Spinning Disc," *Letter in Heat and Mass Transfer*, 1(2), pp. 131–138 (1974).
9. Yakhot, V., Orszag, S. A., Thangam, S., Gatski, T. B. and Speziale, C. G., "Development of Turbulence Models for Shear Flow by a Double Expansion Technique," *Phys. Fluids A*, 4(7), pp. 1510–1520 (1992).
10. Goldberg, U. C., "Exploring a Three-Equation R-κ-ε Turbulence Model," *J. of Fluids Engineering*, 118, pp. 795–799 (1996).
11. Tannehill, J. C., Anderson, D. A. and Pletcher, R. H., "Computational Fluid Mechanics and Heat Transfer," *Taylor & Francis Group*, Chap. 5 (1997).
12. Wilcox, D. C., "Comparison of Two-Equation Turbulence Models for Boundary Layers with Pressure Gradient," *J of AIAA*, 31(8), pp. 1414–1421 (1993).
13. Roe, P. L., "Approximate Riemann Solvers, Parameter Vector, and Difference Schemes," *Journal of Computational Physics*, 43, pp. 357–372 (1981).
14. Tai, C. H., Sheu, J. H. and van Leer, B., "Optimally Multi-Stage Schemes for the Euler Equations with Residual Smoothing," *Journal of AIAA*, 33(6), pp. 1008–1016 (1995).
15. van Leer, B., Thomas, J. L., Roe, P. L. and Newsome, R. W., "A Comparison of Numerical Flux Formulas for the Euler and Navier-Stokes Equations," AIAA Paper 87-1104-cp, pp. 36–39 (1987).
16. Hirsch, C., *Numerical Computation of Internal and External Flow*, A Wiley-Interscience Publication, 2, pp. 460–469 (1989).
17. van Leer, B., "Upwind-Difference Methods for Aerodynamic Problems Governed by the Euler Equations, in Large-Scale Computations in Fluid Mechanics," *Lectures in Applied Mathematics*, 22, pp. 327–336 (1985).
18. van Leer, B., "Upwind-Difference Methods for Aerodynamic Problems Governed by the Euler Equations," *Proceedings of Large-Scale Computations in Fluid Mechanics, Lectures in Applied Mathematics*, 22, pp. 327–336 (1985).
19. Mulder, W. and van Leer, B., "Experiments with Implicit Upwind Methods for the Euler Equations," *Journal of Computational Physics*, 59, pp. 232–246 (1985).
20. van Albada, G. D., van Leer, B. and Roberts, J. W. W., "A Comparative Study of Computational Methods in Cosmic Gas Dynamic," *Astronomy and Astrophysics*, 108, pp. 76–85 (1982).
21. Fromm, E., "A Method for Reducing Dispersion in Convective Difference Scheme," *Journal of Computational Physics*, 3, pp. 413–437 (1968).
22. Hirsch, C., "Numerical Computation of Internal and External Flow," *John Wiley & Sons Ltd.*, 2, Chap. 21 (1990).
23. Goldberg, U. C., "Toward a Pointwise Turbulence Model for Wall-Bounded and Free Shear Flow," *J. of Fluids Engineering*, 116(1), pp. 72–76 (1994).
24. Emmons, H. W., "The Laminar-Turbulent Transition in a Boundary Layer — Part I," *J. of Aerospace Sciences*, 18(7), pp. 490–498 (1951).
25. Clark, J. P., Jones, T. V. and LaGraff, J. E., "On the Propagation of Naturally Occurring Turbulent Spots," *J. of Engineering Mathematics*, 28, pp. 1–19 (1994).
26. Simon, F. F., "The Use of Transition Region Characteristics to Improve the Numerical Simulation of Heat Transfer in Bypass Transitional Flow," *Int. J. of Rotating Machinery*, 2(2), pp. 93–102 (1995).
27. Solomon, W. J., Walker, G. J. and Gostelow, J. P., "Transition Length Prediction for Flow with Rapidly Changing Pressure Gradients," ASME Paper 95-GT-241 (1995).
28. Wang, J., Keller, F. J. and Zhou, D., "Flow and Thermal Structures in a Transitional Boundary Layer," *Experiment Thermal and Fluid Science*, 12, pp. 352–363 (1996).

Table 1 Blade Coordinates

Suction Side		Pressure Side	
X/C	Y/C	X/C	Y/C
0.01414	0.02059	0.01414	0.02059
0.	0.08588	0.05059	0.
0.00353	0.13294	0.09412	0.02682
0.01882	0.18588	0.12941	0.06871
0.05882	0.25035	0.15294	0.08976
0.10588	0.28741	0.17647	0.10506
0.17647	0.31824	0.20588	0.12035
0.24118	0.33271	0.25882	0.14129
0.31176	0.33458	0.32941	0.15647
0.38235	0.32647	0.4	0.16012
0.45296	0.31	0.47059	0.15565
0.52353	0.28647	0.54118	0.14447
0.61176	0.25094	0.61176	0.12941
0.71765	0.20024	0.68235	0.11094
0.82353	0.14318	0.75294	0.08918
0.92941	0.07965	0.82353	0.06412
0.96471	0.05647	0.89412	0.03576
0.98824	0.04059	0.94118	0.01518
1.	0.02118	0.97941	0.
0.99765	0.01059	0.97765	0.01059

(Manuscript received Apr. 16, 2001,
Manuscript revised Nov. 14, 2001,
Accepted for publication Nov. 30, 2001.)